Journal Name

ARTICLE

Alignment of Graphene Nanoplatelets in Poly (vinyl alcohol) Nanocomposite Fibers with Controlled Stepwise Interfacial Exfoliations

Received 00th January 20xx,
Accepted 00th January 20xx

DOI: 10.1039/x0xx00000x

www.rsc.org/

Weiheng Xu[a], Rahul Verma[b], Sayli Jambhulkar[a], Rahul Franklin[b], Kenan Song [c,*]

Hierarchically microstructured tri-axial poly (vinyl alcohol)/grahene nanoplatelets (PVA/GNPs) composite fibers were fabricated using the dry-jet wet spinning technique. The composites with distinct PVA/GNPs/PVA phases led to highly-oriented and evenly-distributed graphene platelets (GNPs) as a result of molecular chain-assisted interfacial exfoliations. With a concentration of 3.3 wt% of the continuously-aligned GNPs, the composite achieved an ~ 66% increase in Young's modulus (~37 GPa) as compared to the pure PVA fiber and a high electrical conductivity of ~0.38 S m^{-1}, one of the highest mechanical/electrical properties reported for polymer/graphene nanocomposites.

Introduction

Polymer-based nanocarbon-included composites have become a highly researched topic in the past few decades for its unique functional properties as well as durability, chemical stability, and low density.[1] More recently, works in 3D printing filaments,[2] functional wearable materials,[3,4] and lightweight robotic textiles[5] continue to push the boundary of such nanocomposites. One-dimensional (1D) carbon nanotubes (CNTs) and two-dimensional (2D) graphene are the most promising nanoparticle reinforcements for their superior mechanical and functional properties.[6789101112] Nevertheless, CNTs-based polymer composites often exhibit much better mechanical properties than those of the graphene-based composites. With similar intrinsic elastic modulus (~1000 GPa) and strength (~100 GPa)[1314] between CNTs and graphene, their distinct enhancement in polymeric matrices are the results of different morphologies and degree of interactions with macromolecules. Previous works mostly focused on uniformly dispersing these nanoparticles in a polymer matrix through solution mixing or in-situ polymerization in order to achieve optimized carbon dispersions.[1516] Effective for 1D nanoparticles due to their one-axis symmetry, 2D platelets or sheets display high-level planar compliance and entropically unstable, leading to surface crumples or folding topologies.[17] Thus, the lack of 2D material microstructural control in the aforementioned methods limits the degree of graphene nanoparticle orientation which eventually leads to inferior composite performances.

Instead of dispersing the nanoparticles in polymer or monomer mixtures, a unique microstructure of separated nanofillers and polymer matrix channels were obtained in our research. In this study, poly(vinyl alcohol) (PVA) was chosen as the polymer matrix for its various properties such as good chemical resistance, biocompatible, hydrophilicity, and processability.[18] Graphene nanoplatelets (GNPs) were chosen as the nanofillers for its 2D features, low cost, and relatively high aspect ratio. Through an in-house designed tri-axial spinneret, a steady flow of the GNPs/solvent suspension constrained by two layers of PVA/solvent solutions was injected during dry-jet wet spinning process to form a sandwiched structure (3-phase). To our knowledge, such configuration has never been reported to demonstrate the orientation behaviors of 2D nanofillers and is expected to be effective on other 2D particles such as boron nitride (BN), molybdenum disulfide (MoS_2), and MXene layers. With pure PVA fiber (1-phase) as controlled samples, 3-phase fiber showed an increase of 66% and 28% in Young's modulus and ultimate tensile strength, respectively. Such configuration also enables the insulating PVA with an electrical conductivity of 0.38 S m^{-1}. Moreover, core-shell structures consisted of continuous GNPs as the core and PVA as the sheath (2-phase) and dispersed GNPs in the PVA matrix (D-phase) were also manufactured to better understand the efficiency and mechanisms of 2D material alignment in 3-phase fibers.

Material and Methods

Materials

[a] System Engineering, The Polytechnic School, Ira A. Fulton Schools of Engineering, Arizona State University, Mesa, AZ, United States 85212
[b] Mechanical Engineering, School for Engineering of Matter, Transport, & Energy (SEMTE), Ira A. Fulton Schools of Engineering, Arizona State University, TEMPE, AZ, United States 85281
[c] * Assistant Professor, The Polytechnic School (TPS) &School for Engineering of Matter, Transport, & Energy (SEMTE), Ira A. Fulton Schools of Engineering, Arizona State University, Mesa, AZ, United States
[d] † Footnotes relating to the title and/or authors should appear here.
Electronic Supplementary Information (ESI) available: [details of any supplementary information available should be included here]. See DOI: 10.1039/x0xx00000x

Graphene nano-platelets (GNPs, grade C-750) was purchased from Sigma Aldrich with a specific area of 750 m^2 g^{-1} and a particle size smaller than 2 µm. Polyvinyl alcohol (PVA, Kuraray 28–98) was obtained from Kuraray with a molecular weight ~ 145,000 g/mol and 98-99% degree of hydrolysis. Methanol, dimethyl sulfoxide (DMSO), n,n-dimethylformamide (DMF, anhydrous, 99.8%), xylene (reagent grade), toluene (anhydrous, 99.8%) were purchased from Sigma-Aldrich (St. Louis, MO, USA) and were used as obtained.

Fiber Spinning

Three spinnerets were designed using Creo Direct Express (Fig. 1$a_{1\text{-}3}$ and Fig. S1) to accommodate one-, two-, and three-phase fiber structures and 3D printed using a fused deposition modeling (FDM) 3D printer (Dimension Elite, Stratasys). Due to limited resolution, the diameter of the channel and the wall thickness were set to 2 mm.

For 3-phase fibers. 20 wt% of PVA polymer pellet was added to DMSO at 120 °C under mechanical stirring for 90 minutes until a clear solution was obtained. 20 wt% of GNPs was added to DMSO and was stirred and tip sonicated for 10 minutes at room temperature. The obtained PVA solution and GNPs dispersion were poured into three syringes. Fig. 1b shows the schematic of the dry-jet wet spinning process, consisting of coagulation, solvent exchange, and heat-drawing. PVA, GNPs, and PVA were connected to inner, middle, and outer outlets, respectively, and were pumped by three syringe pumps at different rates. The composite gel first went through a methanol coagulation bath to form a tri-axial fiber. A winder with a take-up speed of 8m/min was used to collect the fiber to a methanol solvent exchange bath. After 24 hours, the DMSO free fiber was then drawn with two winders at different speeds under 100 °C, 150 °C, and 200 °C stepwise to obtain the final semi-crystalline fiber composite. At each drawing stage, a maximum draw ratio was obtained until any further speed increase of the second winder would result in a breakage.

2-phase fiber. The inner channel of the 2-phase spinneret (Fig. 1a_2) was connected to the same GNPs/DMSO as mentioned above, and the outer channel was connected to the same 20wt% PVA/DMSO solution. Previously mentioned spinning and drawing techniques were used.

1-phase and D-phase fiber. 20 wt% PVA/DMSO was used for 1-phase fiber (Fig. 1a_3), and 4 wt% of GNPs was uniformly dispersed in 20 wt% PVA/DMSO solution for D-phase fiber (Fig. 1a_3). 1-phase spinneret was used for both fibers. Previously mentioned spinning and drawing techniques were used. Fig. 1c shows the four types of fiber structures. More experimental details are listed in Table. S1

Characterization

Fiber morphology was studied using a scanning electron microscopy (SEM) on XL30 ESEM-FEG. Clear cross-sectional areas were cut after cooling the fibers with liquid nitrogen for 5 minutes. 15 nm of gold nanoparticle layers were deposited on the surface to improve conductivity. Thermogravimetric analysis (TGA, LABSYS EVO) was used for 2-phase and 3-phase fibers. The samples were placed in an alumina crucible along with an alumina sample as reference. The chamber was purged with helium gas at 0.5 °C/min for 30 minutes and was heated under a rate of 10 °C/min up to 600 °C. Wide Angle X-ray diffractometer (XRD, Kristallo-Flex 710D X-ray generator, Bruker D5000, Siemens) was used with Cu Kα radiation (40 kV, 40 mA). The scanning range of the Bragg 2θ angle ranged from 5° to 70° under a scanning rate of 2° min^{-1}. Polarized Raman spectroscopy was used with a green laser (532 nm) in the VV configuration where a backscattering light intensity analyzer is set in parallel to the polarized incident laser. The polarized laser beam was scanned from parallel to perpendicular with fiber axial direction. The mechanical properties of the composite fibers were tested with a Discovery HR-2 (TA instruments) at room temperature. 10 samples were tested for each type. The gauge distance was kept at 10 mm and the head-cross speed was set at 100 µm s^{-1}. The electrical conductivity was measured using a multimeter at room temperature and the measured length was set to 2 cm for each fiber. For 3-phase and 2-phase fibers, PVA polymer was scratched at the end to expose the GNPs channel. Silver paste was added to all fiber ends to increase the contact area with the multimeter probe.

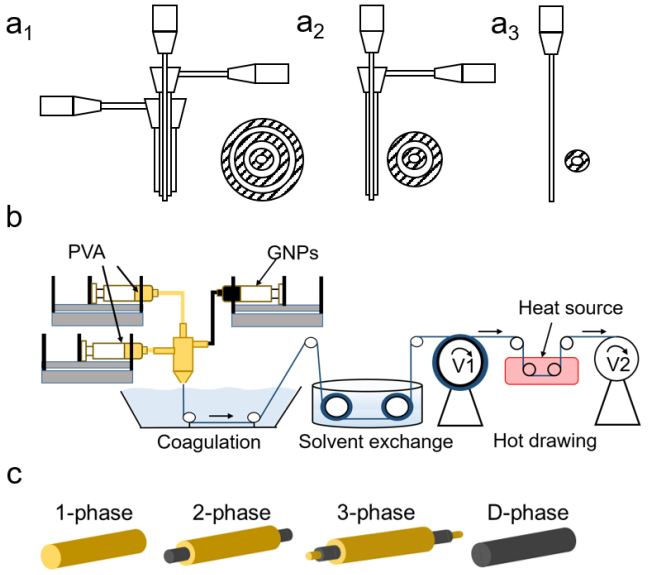

Fig. 1(a1-3) from left to right are the in-house design of the 3-phase, 2-phase, and 1-phase spinnerets with dimensions followed in Fig. S1 and are printed using 3D printer. (b) Dry-jet wet spinning apparatus and procedures, including the spinning dope injection, solvent exchange in coagulation process, and post-treatment of hot-drawing. (c) Four types of fiber microstructures where yellow and black represent PVA polymer and graphene nanoplatelets respectively.

Result and Discussion

Fiber morphology

The dimensions and morphologies of the GNPs can significantly influence their reinforcement effects in polymer matrices. The GNPs used in our research has shown ~13 layers with an aspect ratio of 384.6, which was confirmed by previous research.[19] SEM image suggests a particle size smaller than 2 µm (Fig. S2). The G band and D band in Raman spectra are attributed to the first-order scattering of the E_{2g} vibrational mode in graphite

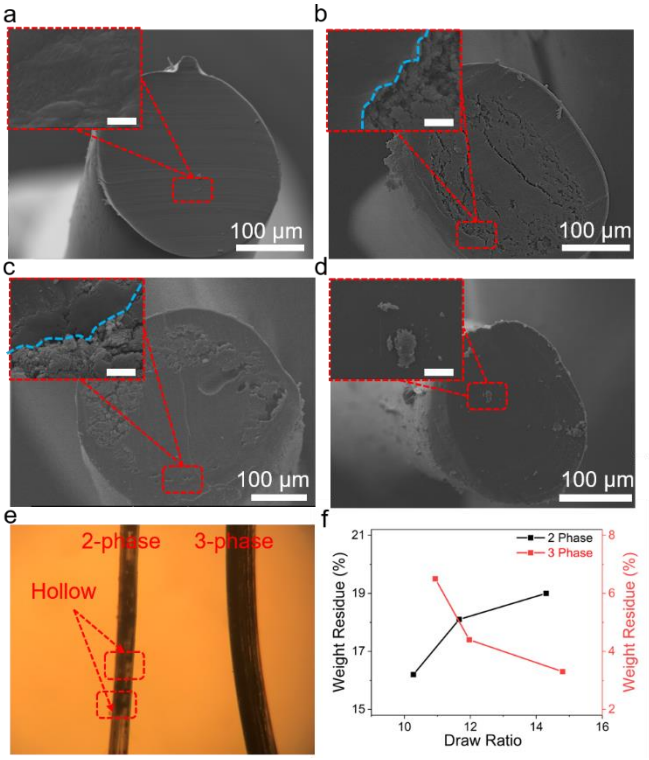

Fig. 2 Morphology and structure characterizations of un-drawn (a) 1-phase, (b) 2-phase with zoomed-in image at the polymer-GNPs interphase, (c) 3-phase with zoomed-in image at the polymer-GNPs interphase, and (d) D-phase fibers with zoomed-in image at the dispersed GNPs. The insert images have a scale bar of 5 μm. (e) Transmitted light microscopy image demonstrates the continuity of GNPs fillers. On the left is the 2-phase fiber and on the right is the 3-phase fiber. (f) TGA analysis on GNPs weight content for the 3-phase fiber and 2-phase fiber as a function of increasing draw ratios.

sheets and structural defect, respectively, and the high ratio between the intensities of D band and G band of the Raman spectra suggests that the GNPs contain relatively high defects (Fig. S3).[20] Due to their tendency to aggregate, the dispersion quality of the GNPs was examined in various solvents including water, toluene, DMSO, DMF, and xylene (Fig. S4). DMSO showed the best dispersion quality for its similar surface energy with graphene, which minimizes the enthalpy of mixing[21]. Notice that our dispersion method has no intention to improve the dispersion quality of GNPs in the solvent with simple 10 mins' tip dispersion but more to prove the facile exfoliation and orientation of graphene materials even at an initially unsatisfying dispersion quality. The cross-sectional morphologies of the as-spun fibers before the post heat treatment were studied using SEM (Fig. 2a-d). As-spun 2-phase and 3-phase fibers (Fig. 2b,c) showed clear phase distinction between GNPs and the polymer channels. Nevertheless, GNPs channel in both fibers exhibit voids as the particles are not densely packed. This is due to the coagulation procedure which the DMSO used to disperse GNPs were exchanged with methanol and spaces occupied by methanol remained unfilled after methanol evaporation. In the after drawn 2-phase fiber, these defects caused crack initiations and propagations during fiber drawing procedures, with hollow cores and uneven graphene segment distributions along the fiber axis (different SEM cross-sections as shown in Fig. S5). On the contrary, 3-phase fibers after heat-drawing displayed high degree of graphene continuity, with a barely visible GNPs channel, indicating a narrowed GNPs channel that is likely the result of exfoliation of the bulk GNPs channel (different SEM cross-sections are shown in Fig. S6). Since PVA are transparent to light, light transmitted microscope image further shows that 2-phase fibers are less continuous than 3-phase fibers with visible hollow cores. (Fig. 2e).

The relationship between GNPs weight ratio with draw ratio

TGA analysis on GNPs weight percentage at various draw ratio also confirmed the step-wise graphene exfoliations (Fig. 2f and Fig. S7). For 2-phase fiber, the GNPs channel has a less tendency to exfoliate and elongate comparing to PVA polymer as its weight percentage increased from 16.2% to 19% increased draw ratio. For 3-phase fiber, GNPs' weight percentage decreased from 6.5% to 3.3% with increased draw ratio. In other words, along with the fiber cross-section area, the comparative graphene channel thickness to polymers increased for 2-phase fibers and decreased for 3-phase fiber. The high difference in weight percentage of the two fibers was also caused by the additional inner polymer layer in the 3-phase fiber. In sum, the decrease in GNPs wt% as a function of drawing temperature in 3-phase fiber proved the step-wise exfoliation of graphene layers; to examine the preferential alignment of graphene, the fiber properties and structures were examined.

Mechanical performance

The stress and strain curves of the post drawn 1-phase, 2-phase, 3-phase, and D-phase fibers are shown in Fig. 3a. The strain for both 1-phase and 3-phase fibers are smaller comparing to 2-phase and D-phase fibers and are likely due to the fact that the fibers are defected which prohibits the polymer chains to be extended to the maximum ratio. Fig. 3b compares the Young's modulus and the tensile strength of the four fiber structures. 3-phase fiber shows an average of 38.8 GPa and 962.9 MPa in Young's modulus and tensile strength, respectively, corresponding to an increase of 73.5% and 17.3% when compared with 1-phase fiber, 22.4 GPa and 821.0 MPa. On the other hand, 2-phase fiber shows inferior modulus and strength of 17.5 GPa and 518.1 MPa. As expected, SEM images suggest the fractures mostly occurred around the voids, as previously discussed, in 2-phase fiber whereas 1-phase and 3-phase fibers show solid fracture cross-sections (Fig. S8). The Young's modulus and strength for the D-phase fiber are 16.7 GPa and 603.2 MPa, respectively. The inferior performance is likely caused by the aggregates and high weight percentage of the GNP nanoparticles shown on the surface of the fiber (Fig. S9). During post drawing, these defects constrain and reduce the mobility of the polymer chains, resulting in the much-lowered draw ratio as well as limited crystallinity. Consequently, the amount of well-dispersed graphene-based materials in composite fibers rarely go beyond 2 weight percent from most literature reports.[82223]

X-ray diffraction analysis of polymeric chains

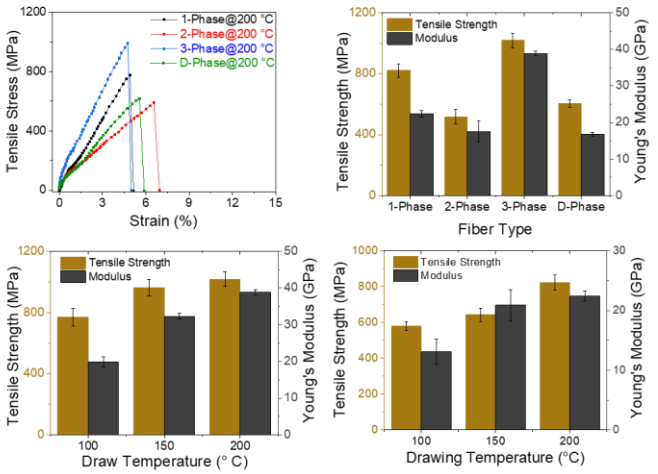

Fig. 3 Mechanical performance of four types of fibers under uniaxial strain. (a) Stress and strain curve. (b) Tensile strength and Young's modulus of four types of fibers after drawing at 200 °C. (c) Strength and modulus of the 3-phase fiber versus drawing temperature. (d) Strength and modulus of the 1-phase fiber versus drawing temperature.

A key to the mechanical performances of polymeric fibers is the degree of polymer orientation which induces higher crystallization and lowers chain entanglement. To study this, crystallite sizes for 1-phase, 2-phase, 3-phase fibers were determined based on X-ray diffraction peak of the (1 0 1) plane using Scherrer's equation (Fig. S10) and they coincident at ~7 nm, indicating the PVA matrix contributed equally on tensile strength in all three samples, thus the reinforcement was mainly contributed by the graphene nanoplatelets. The crystallinities of the PVA matrix were also calculated to be 62%, 64%, and 61% for 1-phase, 2-phase, and 3-phase respectively after 200 ° drawing (Fig. S10), indicating that the exfoliation of the bulk GNPs channel does not have a negatively affect the crystallinity of the PVA channels. A possible reason is that as the bulk GNPs channel is being exfoliated, it contributes a lubrication effect on the overall drawing capability as indicated by the previous study.[24]

GNPs' orientation in 3-phase fiber

The internal structure of the 3-phase fiber was examined by fracturing it under liquid nitrogen to provide qualitative estimation of the platelets' orientations. SEM images show the morphology of the nanoplatelets before and after hot drawing in Fig. 4a and b. Before drawing, the nanoparticles are loosely distributed with no certain orientation. After drawing, the nanoparticles are more closely packed with alignment along the fiber axis indicated by the red arrow.

Raman spectroscopy was further used to quantitatively study the spatial orientation of GNPs. Previous studies have suggested that the 2D band intensity (I_{2D}) of graphene-based materials shows strong angular dependency with the incident light angle.[25262728] A 3-phase fiber sample was set up as shown in Fig. 4a with polarized laser-focused on both the middle and the side sections of the GNPs channel. By rotating the angle, ϕ, between the fiber axis and the polarized laser from 0 to 90 degrees, the obtained Raman spectras are shown in Fig. S11 where the signature D, G, and 2D bands match with the raw

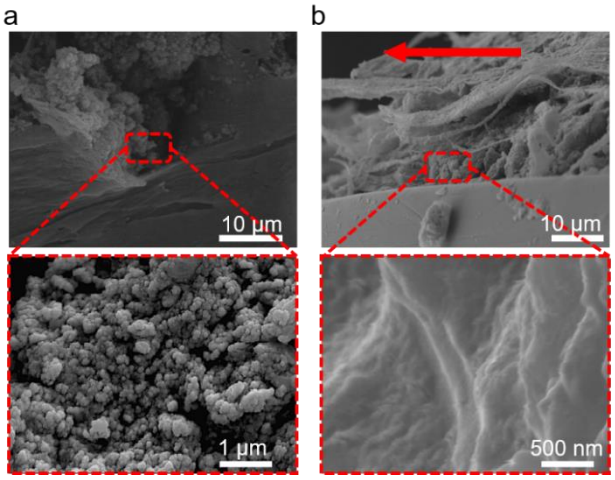

Fig. 4 SEM images of the 3-phase fiber. The boxed regions are enlarged as the lower images. (a) Before drawing and (b) after drawing.

GNPs at ~1350 cm^{-1}, ~1530 cm^{-1}, and ~2750 cm^{-1}. As previous SEM image indicate that the GNPs are aligned along the fiber axis, thus in the case where the laser is focused in the middle section, I_{2D} in does not vary as the incident angle changes (Fig. 5b). On the other hand, when the incident point was focused on the side of the fiber, I_{2D} evidences a decrease in intensity as ϕ increases from 0° to 90°. The normalized intensity is then fitted into an orientation distribution function (ODF)[26], as shown in Fig. 5c and equation 1:

$$I_{GNPs}(\phi) = I_0\left\{\frac{8}{15} + \langle P_2(\cos\theta)\rangle\left(-\frac{16}{21} + \frac{8}{7}\cos^2\theta\right) + \langle P_4(\cos\theta)\rangle\left(\frac{8}{35} - \frac{8}{7}\cos^2\phi + \cos^4\phi\right)\right\} \quad (1)$$

where ϕ is the angle between the fiber axis and the incident laser. $\langle P_2(\cos\theta)\rangle$ and $\langle P_4(\cos\theta)\rangle$ are the second- and fourth-ordered Legendre polynomials with fitted values of 0.55 and 0.67. Usually, $\langle P_2(\cos\theta)\rangle$ is the primary orientation parameter and $\langle P_4(\cos\theta)\rangle$ term is to reconstruct the complete ODF.[26] The plate/spherical shape of the GNPs contributes to the mismatches between the data and the fitted curve since the ODF expression assumes the nanoparticles are uniaxial symmetric.[27] The Krenchel factor, η_0, is a measurement of the nanoparticles orientation, with 1 for perfectly aligned and 1/5 for random 3D orientation. By integrating the ODF over all space, η_0 is shown, as:

$$\eta_0 = \frac{8}{15} + \frac{8}{21}\langle P_2(cos\theta)\rangle + \frac{3}{35}\langle P_4(cos\theta)\rangle \quad (2)$$

By substituting the second- and fourth- Legendre polynomial, η_0 is determined as 0.8.

To explain the high orientation factor of the 3-phase fiber, the proposed microstructure model is shown in Fig. 5d. Before drawing, PVA chains are in an amorphous state, surrounding the misaligned graphene nanoplatelets. The thickness of the GNPs channel is relatively large due to the 3-D printed spinneret outlet dimension. To facilitate graphene orientations, 3-phase fibers were drawn at three different temperatures (100, 150, and 200 °C). As the outer polymer channel in 3-phase fibers began to untangle and extend upon drawing at high temperatures, shear stress would be generated as a

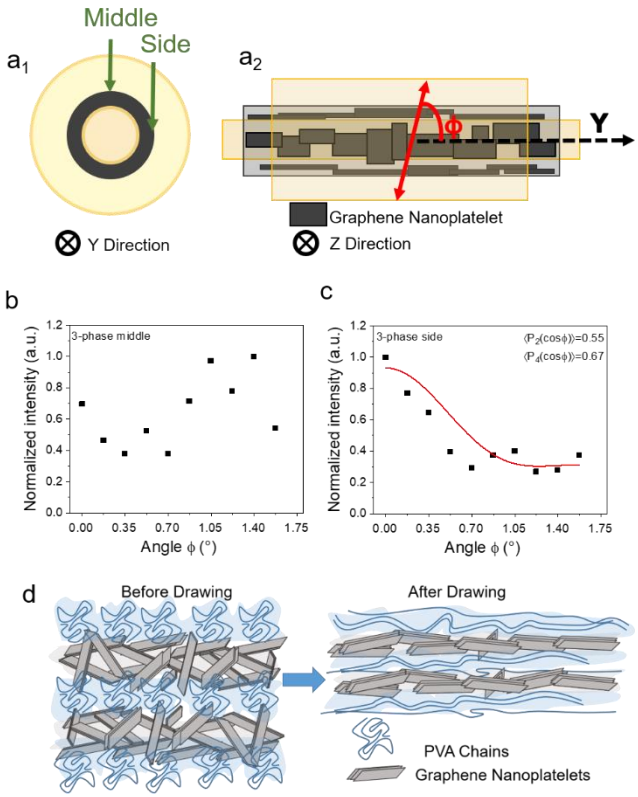

Fig.5 Raman spectroscopy data and illustration of the alignment process. (a_1) Cross-sectional view (along y axis) of the 3-phase fiber showing middle and side region for Raman spectroscopy test. (a_2) Top view (along z axis). (b)The normalized 2D band for middle section showing no obvious angular dependency. (c) The normalized 2D band for side section shows strong angular dependency with $\langle P_2(\cos\theta)\rangle$=0.55 and $\langle P_4(\cos\theta)\rangle$=0.67. (d) Schematics showing the mechanicsm behind the alignment and exfoliation of the GNPs channel.

consequence of comparative movements between outer and inner fiber layers. The polymer surface in contact with the heat zone would be stretched when stress was applied at temperatures above the glass transition point (i.e., 90 °C for PVA). This shear stress, as well as the extension trends, transferred from exterior polymers to graphene channel and would cause step-wise exfoliations of stacked graphene platelets as well as orienting them in the axial direction. The resulting GNPs channel are shown in Fig. 5e, with thinner GNPs channel and better orientation as SEM and Raman spectroscopy suggest.

The effective Young's modulus and tensile strength of the GNPs are also investigated using the modified rule-of-mixture method, as:

$$E_c = \eta_0 V_f E_f + (1 - V_f) E_m \quad (3)$$

$$\sigma_c = \eta_0 V_f \sigma_f + (1 - V_f) \sigma_m \quad (4)$$

where E_c, E_m, E_f, and σ_c, σ_m, σ_f represent the Young's modulus and tensile strength of the composite fiber, polymer matrix, and the GNPs, respectively. V_f is the volume fraction of the GNPs in the composite fiber. By substituting η_0=0.8, E_f is determined to be ~1000 GPa, which corresponds to the theoretical modulus for single-layered graphene.[13] On the other hand, σ_f is determined to be ~11GPa, and it is only 1/9 of the

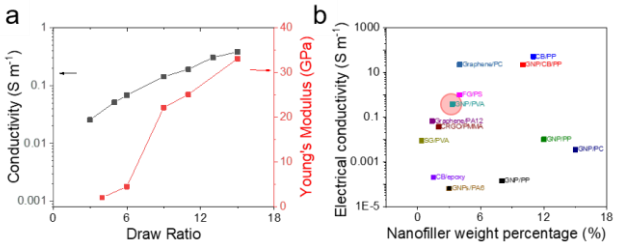

Fig. 6 (a) Electrical conductivity and Young's modulus versus draw ratio for the 3-phase fiber. (b) Comparison of electrical conductivity of our work with selected previous works: GNP/PP,[30,31] GNP/CB/PP,[31] CB/PP,[31] FG/PS,[32] GNP/PC,[33] CB/epoxy,[34] graphene/PA12,[35] CRGO/PMMA,[36] SG/PVA,[37] graphene/PC,[38] GNP/PVA, GNPs/PA6.[39]

theoretical tensile strength of single-layered graphene. One possible reason is that after solvent exchange procedure, the voids due to the evaporated methanol are not fully filled during post drawing, resulting in defects that drastically deteriorate fiber strength performance. Another reason is that the GNPs used are not surface modified, resulting in poor load transfer between them and polymer matrix.

Electrical conductivity of the 3-phase fiber

Different from solution mixing method where 2D and 3D conductive nanoparticles usually lose their 3-dimensional bridged structure upon high ratio drawing,[40] the highly aligned continuous GNPs channel also promotes superior electrical conductivity. Resistance was measured for all types of fibers and conductivity is calculated following equation 5:

$$\sigma = \frac{L}{R\pi r^2} \quad (5)$$

where σ, R, r, and L are electrical conductivity, resistance, fiber radius, and fiber length, respectively. Fig.6a exhibits both Young's modulus and electrical conductivity as a function of draw ratio at room temperature for the 3-phase fiber. Both conductivity and modulus increase with draw ratio, and ultimately reaching 0.38 S m^{-1} while maintaining 38.8 GPa of modulus. This indicates that the alignment of GNPs also enhances the interactions between each platelet, leading to more efficient pathways for electrons. On the other hand, 1-phase, 2-phase, and D-phase fibers show electrical insulation behaviors which are due to the insulating nature of PVA polymer and discrete nanoplatelet particles.

Fig. 6b summarizes some of the previous works on conductivity polymer composite and fibers, and our work is marked in the red circle. Nanofiller weight percentage is closely related to percolation threshold where nanoparticles form an inter-bridged conductive network inside the polymer matrix. However, these particles are usually poorly aligned, resulting in electrons passing through a collection of in-plane and transverse pathways, causing limited conductivity.[41] On the other hand, 3-phase fiber's unique microstructure improves the contact area and facilitates the electron's pathway to be parallel to the surface.

Conclusions

In this work we have successfully demonstrated the advantages in using microstructure to promote improved 2D material's alignment and their exfoliation behaviours. Not only were mechanical properties been enhanced, the 3-phase fiber also demonstrated superior electrical conductivity comparing to other graphene nanoplatelets based fibers and composites. Our work is also capable of using pilot scale production with our 3D printed spinneret that promotes real life applications.

Conflicts of interest

The authors declare no competing financial interest.

Acknowledgements

This work is funded by the start-up fund from Arizona State University (ASU), the Global Sports Institute (GSI), and the U.S. National Science Foundation (NSF).

Notes and references

1 S. Stankovich, D. A. Dikin, G. H. B. Dommett, K. M. Kohlhaas, E. J. Zimney, E. A. Stach, R. D. Piner, S. B. T. Nguyen and R. S. Ruoff, *Nature*, 2006, **442**, 282–286.

2 P. C. Sherrell and C. Mattevi, *Mater. Today*, 2016, **19**, 428–436.

3 S. R. Shin, R. Farzad, A. Tamayol, V. Manoharan, P. Mostafalu, Y. S. Zhang, M. Akbari, S. M. Jung, D. Kim, M. Comotto, N. Annabi, F. E. Al-Hazmi, M. R. Dokmeci and A. Khademhosseini, *Adv. Mater.*, 2016, **28**, 3280–3289.

4 S. Sridar, Z. Qiao, N. Muthukrishnan, W. Zhang and P. Polygerinos, *Front. Robot. AI*, 2018, **5**, 1–9.

5 C. S. Boland, U. Khan, G. Ryan, S. Barwich, R. Charifou, A. Harvey, C. Backes, Z. Li, M. S. Ferreira, M. E. Möbius, R. J. Young and J. N. Coleman, .

6 L. Jin, C. Bower and O. Zhou, *Appl. Phys. Lett.*, 1998, **73**, 1197–1199.

7 S. Mo, L. Peng, C. Yuan, C. Zhao, W. Tang, C. Ma, J. Shen, W. Yang, Y. Yu, Y. Min and A. J. Epstein, *RSC Adv.*, 2015, **5**, 97738–97745.

8 X. Zhao, Q. Zhang, D. Chen and P. Lu, *Macromolecules*, 2010, **43**, 2357–2363.

9 J. Li, L. Shao, X. Zhou and Y. Wang, *RSC Adv.*, 2014, **4**, 43612–43618.

10 Y. Ma, D. Bai, X. Hu, N. Ren, W. Gao, S. Chen, H. Chen, Y. Lu, J. Li and Y. Bai, *ACS Appl. Mater. Interfaces*, 2018, **10**, 3002–3010.

11 W. Qin, F. Vautard, L. T. Drzal and J. Yu, *Compos. Part B Eng.*, 2015, **69**, 335–341.

12 U. Khan, K. Young, A. O'Neill and J. N. Coleman, *J. Mater. Chem.*, 2012, **22**, 12907–12914.

13 C. Lee, X. Wei, J. W. Kysar and J. Hone, *Science (80-.).*, 2008, **321**, 385–388.

14 J. P. Lu, *J. Phys. Chem. Solids*, 1997, **58**, 1649–1652.

15 L. C. Tang, Y. J. Wan, D. Yan, Y. B. Pei, L. Zhao, Y. B. Li, L. Bin Wu, J. X. Jiang and G. Q. Lai, *Carbon N. Y.*, 2013, **60**, 16–27.

16 J. Liang, Y. Huang, L. Zhang, Y. Wang, Y. Ma, T. Cuo and Y. Chen, *Adv. Funct. Mater.*, 2009, **19**, 2297–2302.

17 T. Ramanathan, A. A. Abdala, S. Stankovich, D. A. Dikin, M. Herrera-Alonso, R. D. Piner, D. H. Adamson, H. C. Schniepp, X. Chen, R. S. Ruoff, S. T. Nguyen, I. A. Aksay, R. K. Prud'Homme and L. C. Brinson, *Nat. Nanotechnol.*, 2008, **3**, 327–331.

18 C. Shao, H. Y. Kim, J. Gong, B. Ding, D. R. Lee and S. J. Park, *Mater. Lett.*, 2003, **57**, 1579–1584.

19 J. G. Um, Y. S. Jun, H. Alhumade, H. Krithivasan, G. Lui and A. Yu, *RSC Adv.*, 2018, **8**, 17091–17100.

20 A. C. Ferrari, *Solid State Commun.*, 2007, **143**, 47–57.

21 Y. Hernandez, V. Nicolosi, M. Lotya, F. M. Blighe, Z. Sun, S. De, I. T. McGovern, B. Holland, M. Byrne, Y. K. Gun'ko, J. J. Boland, P. Niraj, G. Duesberg, S. Krishnamurthy, R. Goodhue, J. Hutchison, V. Scardaci, A. C. Ferrari and J. N. Coleman, *Nat. Nanotechnol.*, 2008, **3**, 563–568.

22 S. R. Ahmad, R. J. Young and I. A. Kinloch, *Int. J. Chem. Eng. Appl.*, 2015, **6**, 1–5.

23 A. Bisht, K. Dasgupta and D. Lahiri, *J. Appl. Polym. Sci.*, 2018, **135**, 1–11.

24 K. Song, Y. Zhang, J. Meng and M. L. Minus, *J. Appl. Polym. Sci.*, 2013, **127**, 2977–2982.

25 Q. Liang, X. Yao, W. Wang, Y. Liu and C. P. Wong, *ACS Nano*, 2011, **5**, 2392–2401.

26 Z. Li, R. J. Young, I. A. Kinloch, N. R. Wilson, A. J. Marsden and A. P. A. Raju, *Carbon N. Y.*, 2015, **88**, 215–224.

27 Z. Li, R. J. Young, N. R. Wilson, I. A. Kinloch, C. Vallés and Z. Li, *Compos. Sci. Technol.*, 2016, **123**, 125–133.

28 H. G. Chae, M. L. Minus and S. Kumar, *Polymer (Guildf).*, 2006, **47**, 3494–3504.

29 Y. A. Badr, K. M. Abd El-Kader and R. M. Khafagy, *J. Appl. Polym. Sci.*, 2004, **92**, 1984–1992.

30 P. Steurer, R. Wissert, R. Thomann and R. Mülhaupt, *Macromol. Rapid Commun.*, 2009, **30**, 316–327.

31 E. Nilsson, H. Oxfall, W. Wandelt, R. Rychwalski and B. Hagström, *J. Appl. Polym. Sci.*, 2013, **130**, 2579–2587.

32 S. NK and M. RM, *J. Appl. Polym. Sci.*, 2008, **109**, 3991–3999.

33 J. A. King, M. D. Via, F. A. Morrison, K. R. Wiese, E. A. Beach, M. J. Cieslinski and G. R. Bogucki, *J. Compos. Mater.*, 2012, **46**, 1029–1039.

34 F. H. Gojny, M. H. G. Wichmann, B. Fiedler, I. A. Kinloch, W. Bauhofer, A. H. Windle and K. Schulte, *Polymer (Guildf).*, 2006, **47**, 2036–2045.

35 D. Yan, H. Bin Zhang, Y. Jia, J. Hu, X. Y. Qi, Z. Zhang and Z. Z. Yu, *ACS Appl. Mater. Interfaces*, 2012, **4**, 4740–4745.

36 X. Zeng, J. Yang and W. Yuan, *Eur. Polym. J.*, 2012, **48**, 1674–1682.

37 R. K. Layek, S. Samanta and A. K. Nandi, *Carbon N. Y.*, 2012, **50**, 815–827.

38 M. Yoonessi and J. R. Gaier, *ACS Nano*, 2010, **4**, 7211–7220.

39 B. A. Weise, K. G. Wirth, L. Völkel, M. Morgenstern and G. Seide, *Carbon N. Y.*, 2019, **144**, 351–361.

40 J. W. Kim and J. S. Lee, *Fibers Polym.*, 2017, **18**, 81–87.

41 S. Wu, R. B. Ladani, J. Zhang, E. Bafekrpour, K. Ghorbani, A. P. Mouritz, A. J. Kinloch and C. H. Wang, *Carbon N. Y.*, 2015, **94**, 607–618.